MEASUREMENTS OF INGRESS IN UPSTREAM AND DOWNSTREAM TURBINE WHEEL-SPACES

M. Patinios - J. A. Scobie - C. M. Sangan - G. D. Lock

Department of Mechanical Engineering, University of Bath, Bath, United Kingdom, BA2 7AY

ABSTRACT

This paper presents measurements of concentration and pressure in a new, highly instrumented and versatile, 1.5-stage gas turbine facility. The rig, which has been specifically designed for investigations related to hot gas ingestion, features interchangeable rim-seals, blading configurations and the capability of operating at a wide range of flow coefficients. The turbine section includes an upstream and a downstream wheel-space on either side of a rotor disc featuring turned blades.

Measurements of CO_2 concentration and steady static pressure were used to assess the pressure field in the turbine annulus and to investigate the performance of a radial clearance rim seal in both wheel-spaces. The wealth of data presented will be of great significance for CFD validation studies considering downstream cavities. Pressure measurements were made at various locations in the turbine annulus for a range of flow coefficients. In the annulus upstream of the rotor blades $\Delta C_p^{1/2}$, the non-dimensional pressure difference, was shown to increase linearly with C_F. Downstream however, $\Delta C_p^{1/2}$ reaches a minimum at a C_F close to the operating point. The radial variation in concentration effectiveness in the upstream and downstream wheel-spaces is provided for a range of sealing flow rates. In both cases the concentration on the stator walls was virtually invariant with radius and equal to that in the rotating core. The results also showed that for the same effectiveness, a smaller value of non-dimensional sealing flow is required in the downstream wheel-space, indicating a weaker driver for ingress.

KEYWORDS

INGRESS, SEALING, CAVITY FLOWS

NOMENCLATURE

b	radius of seal (m)
c	concentration of tracer gas
C_F	flow coefficient [$= W/\Omega b$]
$C_{p,a}$	pressure coefficient in annulus [$= p_a - \bar{p}_a / \frac{1}{2}\rho\Omega^2 b^2$]
$C_{w,0}$	nondimensional sealing flow rate [$= \dot{m}/\mu b$]
G	gap ratio [$= S/b$]
G_c	seal-clearance ratio [$= s_{c,ax}/b$]
$\dot{m}$	mass flow rate (kg/s)
k_a	empirical constant
M	Mach number
p	static pressure (Pa)
r	radius (m)
Re_w	axial Reynolds number in annulus based on radius [$= \rho W b/\mu$]
Re_ϕ	rotational Reynolds number [$= \rho\Omega b^2/\mu$]
s_c	seal clearance (m)
S	axial clearance between rotor and stator (m)
U	bulk mean radial seal velocity [$= \dot{m}_0/2\pi\rho b s_c$]
W	axial velocity in annulus (m/s)
z	axial coordinate in wheel-space (m)
ε_c	concentration effectiveness
Φ_0	non-dimensional sealing parameter [$= U/\Omega b$]
Φ_{min}	minimum value of Φ_0 to seal wheel-space
Φ_{min}'	value of Φ_0 when $\varepsilon_c = 0.95$
λ_T	turbulent flow parameter [$= C_{w,0}\,\mathrm{Re}_\phi^{-0.8}$]
μ	dynamic viscosity (kg/ms)

ρ	density (kg/m^3)	Ω	angular speed of rotating disc (rad/s)

Subscripts

a	annulus	*rad*	radial
ax	axial	*0*	sealing flow
min	minimum	*s*	stator surface

INTRODUCTION

Gas turbines are widely employed in applications ranging from aircraft propulsion to the generation of electrical power. Faced with increasing fuel costs and ever more stringent environmental legislation, engine manufacturers must design machines with improved efficiency in order to compete on the global stage. One way of increasing engine efficiency is to raise the turbine entry temperature (TET). Modern gas turbines operate with TETs substantially above the melting temperature of the materials used in their construction. In order to operate at these elevated temperatures gas turbines are *air-cooled*; air is bled from the compressor and reintroduced within the turbine to cool critical components. There exists an intricate balance between effective cooling and superfluous use, which must be optimised in order to avoid unnecessary performance penalties.

A key challenge facing the designer is the ingestion of hot mainstream gases within the disc cavities formed between adjacent stationary (*stator*) and rotating (*rotor*) discs. Rim seals, such as that shown in Fig. 1, are fitted at the periphery of the disc cavity (or *wheel-space*). These seals can vary greatly in their geometry and configuration; typical high-pressure gas turbines feature rim-seals designed to be appropriate for each disc face and stage (Fig.1 illustrates a characteristic seal arrangement).

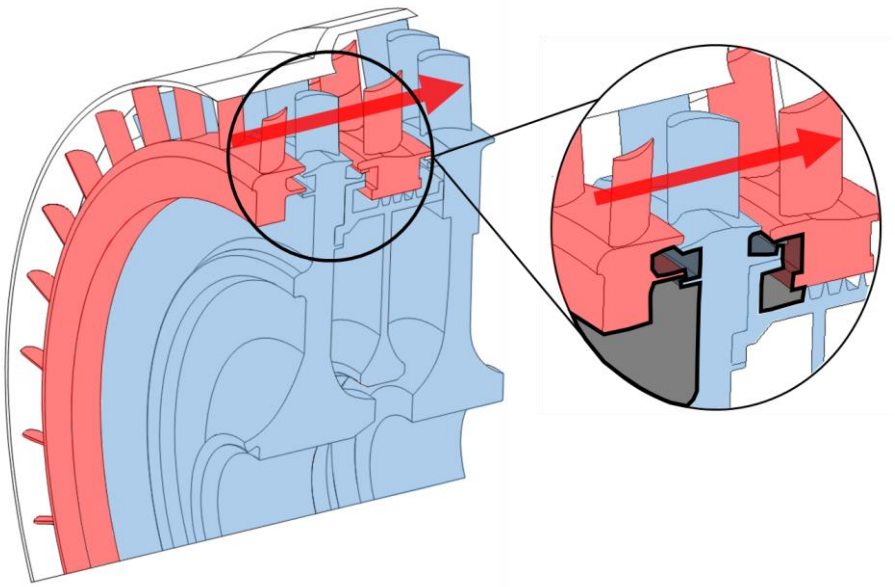

Figure 1: A typical gas turbine stage; rim-seals, highlighted in black, are shown inset (red highlight: stationary discs; blue highlight: rotating discs)

Engine manufacturers use advanced computational fluid dynamic (CFD) simulations to design increasingly complex rim-seals; CFD simulations of the unsteady and three-dimensional flow present in the mainstream gas-path and cooling systems of gas turbines are computationally expensive. Simulations rely heavily on the insight and validation provided by experimental work, often conducted in test rigs operating in controlled conditions. Experimental facilities range from near-engine representative stages to rigs operating at relatively benign conditions. The latter offers the benefit of improved instrumentation capability, accuracy, flexibility and expediency.

This paper presents the performance capability of a new, versatile and highly instrumented 1.5-stage turbine experimental facility specifically built for investigations of hot gas ingestion. The

annulus pressure field is examined at various operating conditions with regards to its effect on ingestion; experimental measurements of rim-seal effectiveness are presented to support the conclusions.

ROTOR-STATOR SYSTEMS

Hot gas ingestion occurs as a result of a pressure difference between the gas turbine annulus and that in the wheel-space. The vanes and blades create an unsteady circumferential distribution of pressure radially outward of the rim-seals; ingress occurs where the pressure in the annulus is higher than in the wheels-space, egress occurs *vice-versa*. This was coined by Owen *et al.* (2011b) as *externally-induced* (EI) ingress.

The flow structure found in the wheel-space is governed by separate boundary layers on both the stator and rotor, between which exists a rotating inviscid core. The rotating fluid creates a radial gradient of pressure, whereby the pressure increases towards the rim seal. Owing to the pressure gradient, fluid can be drawn into the wheel-space even in the absence of any external pressure asymmetry. This form of ingestion was coined *rotationally-induced* (RI) ingress by Owen *et al.* (2011a). In certain circumstances the effects of EI and RI are both significant: this is termed *combined* (CI) ingress.

Fluid structure in the wheel-space

Figure 2 shows the flow structure in the upstream and downstream wheel-spaces for the case where there is a superposed sealing flow, with swirl, together with ingestion through the rim-seal.

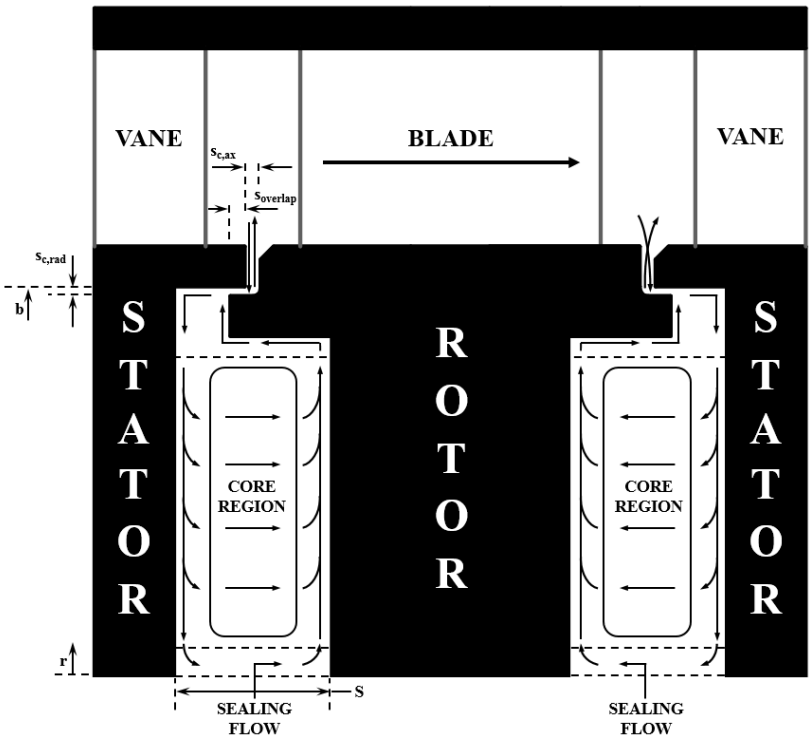

Figure 2: Flow structure expected in the upstream and downstream wheel-spaces (based on Patinios *et al.* (2016))

Consider first the upstream wheel-space. The discs are wide enough apart that separate boundary layers form on each of them, both of which start at entry to the wheel-space. Fluid moves radially outward in the boundary layer on the rotor and inward in the boundary layer on the stator. Over much of the wheel-space, fluid is entrained axially across the rotating inviscid core from stator to rotor. Owing to the Taylor-Proudman theorem (documented by Childs (2011), all radial flow is confined to the boundary layers on the rotor and stator discs. The sealing flow is introduced to the system in an

inner region (shown in Fig. 2 between two dashed lines), by which point all the available flow will have become entrained in to the rotor boundary layer. In the outer region (radially outward of the outmost dashed line on Fig. 2), some fluid flows from the rotor to the stator, while the remainder leaves the system as egress through the rim seal.

An extensive review of computational, theoretical and experimental modelling of hot gas ingestion – including those works relating to flow structure – is provided by Scobie *et al.* (2016). The majority of these studies focus on ingress in the *upstream* wheel-space of a gas turbine; far fewer investigators have conducted detailed studies downstream of the rotor.

Patinios *et al.* (2016) presented the first experimental data from the test facility used in this paper. The authors were able to investigate the expected flow structure in the downstream wheel-space and draw comparisons with the established structure widely accepted upstream of the rotor. The study concluded that the flow structure was broadly similar in both wheel-spaces, however an important difference was noted in the vicinity of the rim seal.

In the downstream wheel-space the ingested fluid has to cross an axis-symmetric "*curtain*" of egress before entering the wheel-space (shown in Fig. 2). The subsequent exchange of angular momentum between the two streams is expected to attenuate any pressure asymmetries and result in an increased sealing effectiveness downstream of the rotor. Experimental measurements conducted by the authors using *double* radial-clearance seals provided supporting evidence for this theory; this paper continues the investigation with *single* radial-clearance seals.

Governing Non-Dimensional Parameters for Ingress

The ingress of fluid through the rim-seal is an inertial phenomenon driven by differences in pressure, whereas the flow inside the wheel-space is controlled by the boundary-layers on the rotor and stator. Defined below are two non-dimensional flow rates (Φ_0 and λ_T) which respectively govern these inviscid and viscous phenomena.

The sealing flow parameter, Φ_0, combines the effects of $C_{w,o}$, G_c and Re_Φ into a single variable:

$$\boldsymbol{\Phi_0 = \frac{C_{w,0}}{2\pi G_c Re_\phi} = \frac{U}{\Omega b}} \qquad \textbf{(Eq. 1)}$$

where U is the bulk mean radial velocity of sealing air through the seal clearance. As both Re_ϕ and $C_{w,0}$ include viscous terms which cancel, Φ_0 is therefore an inertial parameter.

The structure of the flow in the wheel-space is determined by the turbulent flow parameter (governing a viscous phenomenon), which is defined as:

$$\boldsymbol{\lambda_T = C_{w,0} Re_\phi^{-0.8}} \qquad \textbf{(Eq. 2)}$$

THE 1.5-STAGE GAS TURBINE TEST FACILITY

Facility Overview

A component view of the test facility is shown in Figure 3. Compressed air from a coaxial inlet pipe is supplied to the gas turbine annulus through a radial diffuser. The radial diffuser features 32 flow guides (one per vane) in which the flow transitions through an increase in radius, while promoting an equal flow distribution. The mainstream flow subsequently passes through 32 removable inlet pipes before entering an annular transition; carbon fibre inserts within the transition piece create an axisymmetric inlet to the turbine stage.

The turbine assembly consists an upstream stator with 32 vanes, a rotor with 48 turned blades and a downstream stator with a further 32 vanes. The stators are manufactured as bladed rings, or *blings*, allowing for the installation of radial-assembly seals; the rotor is manufactured as a *blisc*. The rotor disc can be rotated at speeds up to 4000 rpm by a 34 kW drive-and-brake dynamometer, required to absorb the power generated from the rig. The downstream stator assembly is supported on a

cantilevered bearing housing, and a hydraulic coupling was used to mount the rotor to the driveshaft. A flexible coupling between the driveshaft and dynamometer is used to isolate the turbine assembly from vibrations.

Sealing flow is supplied axially to the upstream and downstream wheel-spaces at low radius, through inlet seals (shown in Figure 3, *inset*). Thermal mass-flow meters and close-coupled control valves were used to control the mass flows to the test rig; all mass-flows were measured to an accuracy of +/- 1% of the full-scale range.

For a more comprehensive description of the experimental facility the reader is directed to Patinios *et al.* (2016) and Scobie (2014).

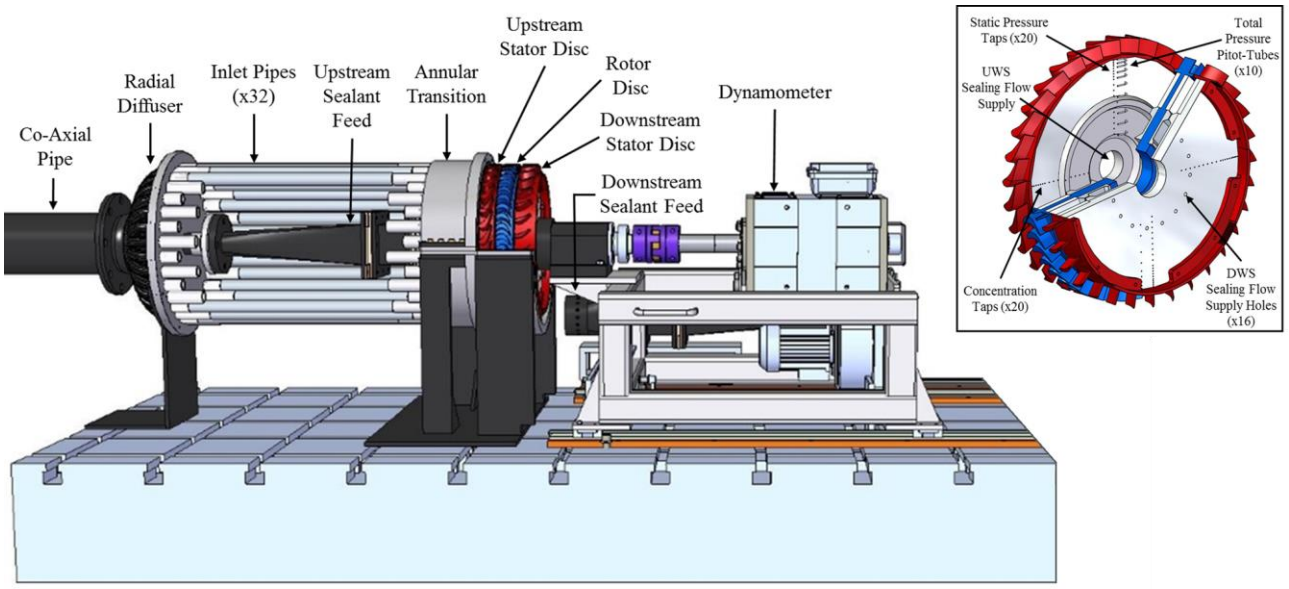

Figure 3: Component view of the experimental facility (some of the inlet pipes and the annulus casing are removed in order to aid clarity); details of the stage and salient instrumentation are shown inset.

Operating Conditions

Table 1 shows the operating conditions of the 1.5-stage test facility. In this study experiments were performed at a maximum speed of 4000 rpm, creating a rotational Reynolds number $Re_\phi = 1.0 \times 10^6$. Despite the maximum Re_ϕ being an order of magnitude smaller than that typically found in engines, the flow structure in rotor-stator systems is principally governed by the turbulent flow parameter λ_T and depends only weakly on Re_ϕ (Owen and Rogers (1989)). In modern engines λ_T is typically less than 0.22 (Scobie *et al.* (2016)); $\lambda_T < 0.22$ in all experiments presented in this study.

The mass-flow rate supplied to the turbine annulus can be controlled so that a wide range of flow coefficients, C_F, can be achieved. The *operating* flow coefficient for the test facility is $C_F = 0.34$; *off-design* is used to describe experiments where $C_F \neq 0.34$. The operating condition resulted in a maximum axial Reynolds Number, $Re_w = 3.4 \times 10^5$ and a corresponding Mach number at the exit of the upstream stator vanes of M = 0.37. The *degree of reaction* for all experiments is 12.5%.

Parameters	**Disc Speed (RPM)**	
	3000	**4000**
Rotational Reynolds Number, $\boldsymbol{Re_\phi}$	7.2×10^5	1.0×10^6
Axial Reynolds Number, $\boldsymbol{Re_w}$	2.4×10^5	3.4×10^5
Flow Coefficient, $\boldsymbol{C_F}$	0.34	
Vane Exit Mach Number, **M**	0.28	0.37

Table 1: Test rig operating points

Experimental Measurements

Measurements of CO_2 concentration, static and total pressure can be taken at various locations in the annulus and in the upstream and downstream wheel-spaces, as shown in Fig. 3.

The variation of steady static pressure with non-dimensional vane pitch was measured at ten discrete locations in the turbine annulus: four axial locations on the hub (A1 to A4) and six further locations on the outer shroud (B1 to B6), shown in Figures 5-8. Dimensioned positions of each location are shown in Figure 6. At each location there were 15 pressure taps across a vane pitch, with a duplicate set positioned at 180° around the azimuth in each case in order to assess repeatability (a total of 300 sampling locations). All static pressure measurements were made using four, 48-channel Scani-Valves, fitted with differential pressure transducers with an accuracy of ±0.3% of the measurement range.

The degree of ingress, and subsequently the sealing effectiveness, ε_c, of rim-seals was determined using measurements of CO_2 concentration. The sealing flow was seeded with 1% CO_2 prior to entry into either wheel-space, c_0, while the mainstream flow in the annulus (measured directly upstream of the first row of stator vanes) was kept unseeded and monitored as c_a. The relative dilution of the seeded sealing flow could be measured at 20 radial positions on each stator disc; the concentration of CO_2 on the stator wall, c_s, was then used to define the *concentration effectiveness,* ε_c, as follows:

$$\boldsymbol{\varepsilon_c = \frac{c_s - c_a}{c_0 - c_a}} \qquad \textbf{(Eq. 3)}$$

The concentration in the rotating core, c_∞, was measured in both wheel-spaces, at ten discrete radial locations, using pitot tubes as sampling inlets (shown in Fig. 3); the pitot tubes were positioned axially at z/S = 0.25 and aligned tangentially to the oncoming flow. Concentration measurements were made using a two-channel Signal Group 9000MGA gas analyser with repeatability and linearity of better than 1 % and 0.5 % of the full-scale range, respectively.

Geometry of Single Radial-Clearance Seals

The geometric configuration of the single radial-clearance rim-seals is shown in Figure 2; key parameters are annotated in the figure. The single radial-clearance seal consists of a rotor-side lip that forms an axial overlap underneath the stator hub, $s_{overlap}$, of 1.86 mm. The seal creates a radial-clearance with the stator hub, $s_{c,rad}$, of 1.28 mm; the axial clearance between the rim at the periphery of the wheel-space, $s_{c,ax}$ is 2 mm. All nominal seal clearances were measured under static conditions within +/- 0.05 mm. The gap ratio, G = 0.1, ensures a turbulent flow structure and separated boundary layers in the wheel-spaces (Daily and Nece (1960)). The height of the annulus, h, is 25 mm.

EXPERIMENTAL RESULTS

Annulus Pressure Measurements

The circumferential distribution of $C_{p,a}$ across two non-dimensional vane pitches is shown in Figure 4 at location A_1 (upstream vane platform) and A_4 (downstream vane platform). The measurements were made for the case of no sealing flow, i.e. Φ_0 = 0. The asymmetry in pressure at location A_1 is caused by the potential field of the upstream vane. In contrast, the A_4 measurements demonstrate the influence of the bow-wave that propagates forward from the downstream vane leading edge. It can been seen that the non-dimensional peak-to-trough pressure difference, $\Delta C_{p,a}$ (defined in the figure), is greater upstream than that downstream.

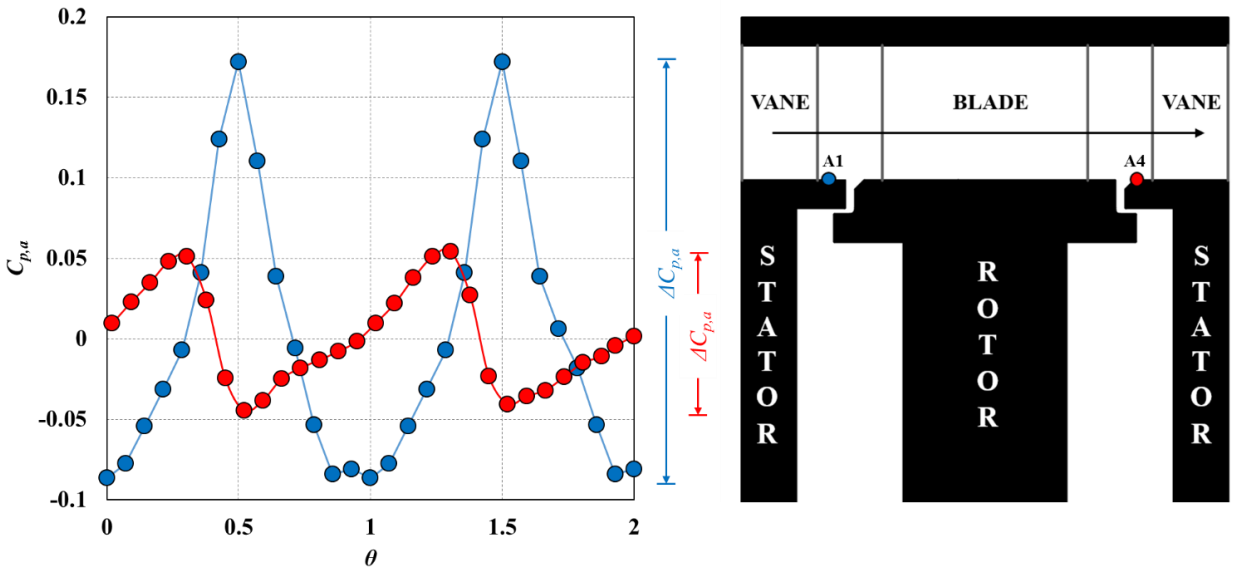

Figure 4: Non-dimensional pressure coefficient in the annulus, $C_{p,a}$, at locations A_1 and A_4 (C_F = 0.34, Re_ϕ = 7.2 × 10^5, Φ_0 = 0)

Figure 5 shows how $\Delta C_{p,a}$ varies in the annulus at all of the measurement locations. Upstream of the rotating blades at both the vane platform (A locations) and outer shroud (B locations), $\Delta C_{p,a}$ decreases with axial distance, x. The difference in peak-to-trough pressure decays with axial distance from the upstream vane trailing edge. The downstream measurements show $\Delta C_{p,a}$ increases as the vane leading edge is approached and the effect of the bow-wave is intensified. For both the upstream and downstream measurements a difference in $\Delta C_{p,a}$ can be observed when comparing the results taken at the same axial location on the vane platform and outer shroud, e.g. A_1 with B_1 and A_3 with B_5. Swirl in the annulus causes a radial pressure gradient which results in larger $\Delta C_{p,a}$ values at the outer locations. Figure 5 highlights that $\Delta C_{p,a}$ depends on where in the annulus it is measured.

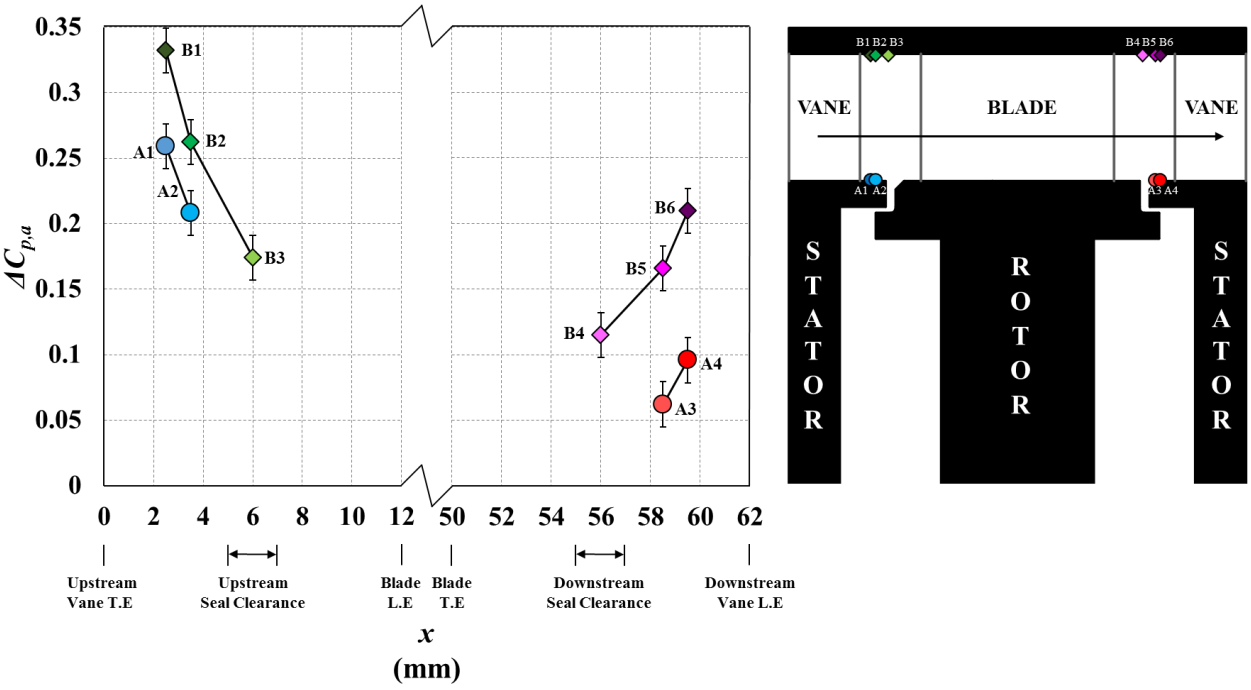

Figure 5: Variation of annulus circumferential pressure asymmetry (C_F = 0.34, Re_ϕ = 7.2 × 10^5, Φ_0 = 0)

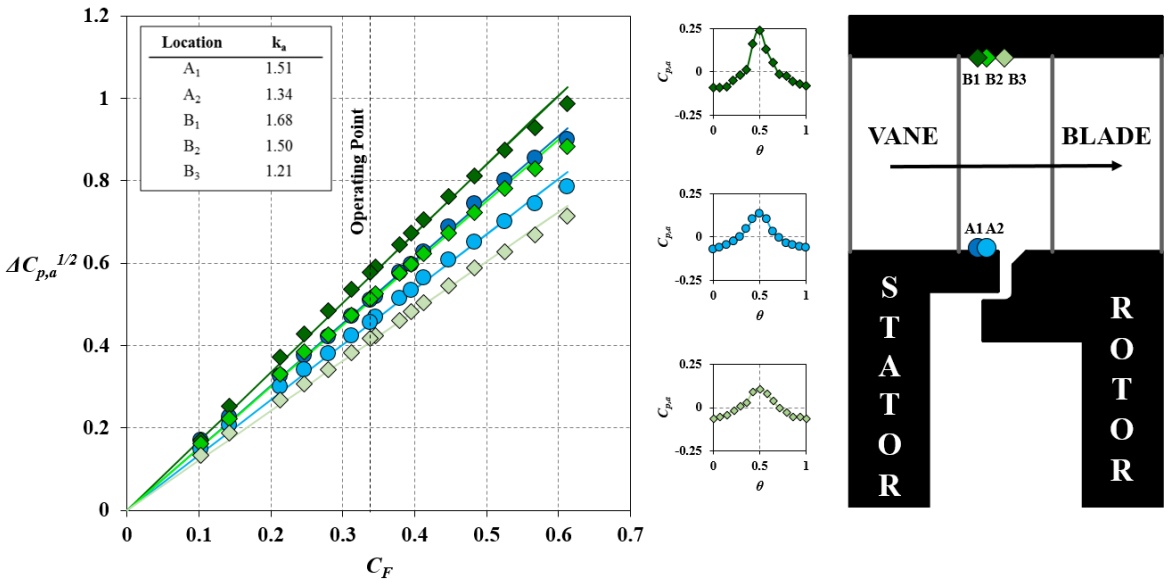

Figure 6: Variation of $\Delta C_{p,a}^{1/2}$ with flow coefficient C_F in the annulus upstream of the rotor blades and selected circumferential distributions of non-dimensional pressure coefficient, $C_{p,a}$ at the operating point, ($Re_\phi = 7.2 \times 10^5$, $\Phi_0 = 0$)

Figure 6 shows the variation of $\Delta C_{p,a}^{1/2}$ with flow coefficient, C_F in the annulus upstream of the rotating blades at locations A_1, A_2, B_1, B_2 and B_3. For all measurement locations $\Delta C_{p,a}^{1/2}$ increases linearly with C_F. The amount of ingestion of mainstream flow in the upstream wheel-space is therefore expected to increase as C_F increases. The variation of $\Delta C_{p,a}^{1/2}$ with C_F was correlated by

$$\Delta C_{p,a}^{1/2} = k_a C_F \qquad \textbf{(Eq. 4)}$$

where k_a an empirical constant representing the gradient of the straight lines. The values of k_a at the various measurement locations are provided in the table within the figure. Also shown in Figure 6 is the variation of non-dimensional pressure, $C_{p,a}$ across one vane pitch at the operating point where C_F = 0.34 for locations A_2, B_1 and B_3.

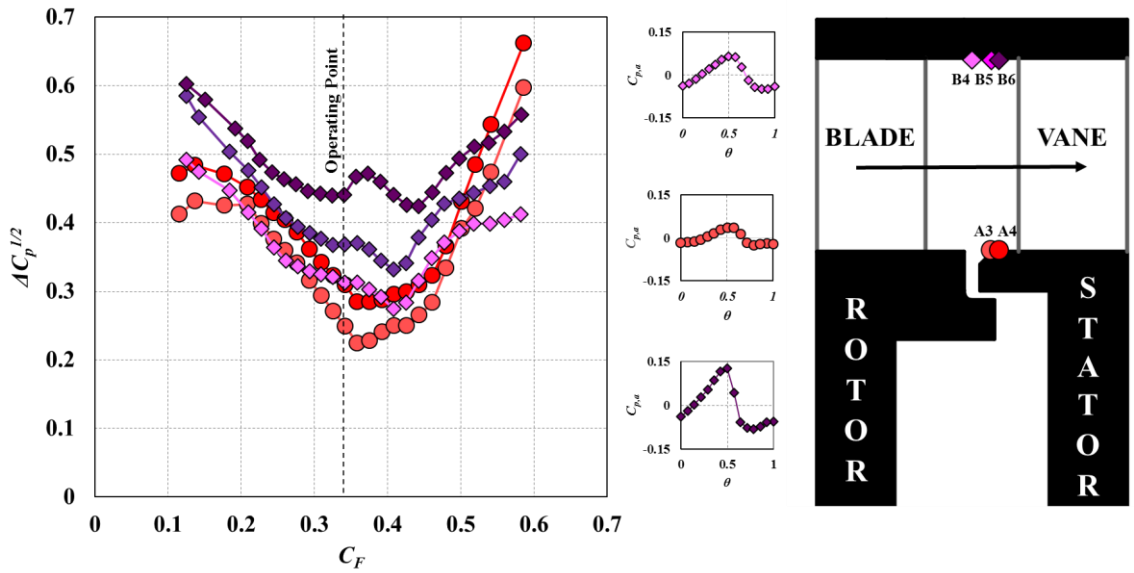

Figure 7: Variation of $\Delta C_{p,a}^{1/2}$ with flow coefficient C_F in the annulus downstream of the rotor blades and selected circumferential distributions of non-dimensional pressure coefficient, $C_{p,a}$ at the operating point, ($Re_\phi = 7.2 \times 10^5$, $\Phi_0 = 0$)

Figure 7 shows the variation of $\Delta C_{p,a}^{1/2}$ with C_F in the annulus downstream of the rotating blades, at locations A_3, A_4, B_4, B_5 and B_6; unlike the upstream variation the relationship is clearly not linear. For all locations $\Delta C_{p,a}^{1/2}$ reaches a minimum at a flow coefficient close to the operating point, where the flow velocity triangles are aligned with inlet angle of the downstream vane. Either side of this the blockage increases as the flow impinges on the vane causing an increase in pressure. The outer shroud locations will also be affected by the blade tip clearance and the corresponding leakage flow. Once again a selection of $C_{p,a}$ variations across one downstream vane pitch are also shown for locations A_3, B_4 and B_6.

Wheel-Space Concentration Measurements

Radial Distribution of Effectiveness

Figure 8 shows the radial variation of ε_c in the upstream and downstream wheel-spaces for the single radial-clearance seal. The measurements were taken on the stator surfaces (circle symbols) and in the rotating-core (diamond symbols) at $z/S = 0.25$ using sampling probes. The experiments were conducted for several values of Φ_0 and hence λ_T; in all cases ingress occurred. In both wheel-spaces ε_c on the stator wall and in the core increases as Φ_0 increases and the sealing flow raises the pressure in the wheel-space relative to the annulus.

For all sealant flow rates the effectiveness in the stator boundary layer and in the rotating core is broadly invariant with radius for $r/b \geq 0.65$. Measurements of the variation of sealing effectiveness, ε_c with non-dimensional sealing flow rate, Φ_0 are expected to be independent of radial location as the stator side boundary layer is non-entraining. In all cases the effectiveness in the rotating core is found to be equal to that of the stator boundary layer with the exception of $r/b = 0.993$ in the upstream wheel-space. This region is characterised by intense mixing of angular momentum and concentration. The egress will be pumped up through the rotor boundary layer (with high ε_c) and the ingress will enter the wheel-space on the stator side (with low ε_c). All of the results are in agreement with the findings of Patinios *et al.* (2016) and provide evidence for a similar flow structure in the two wheel-spaces.

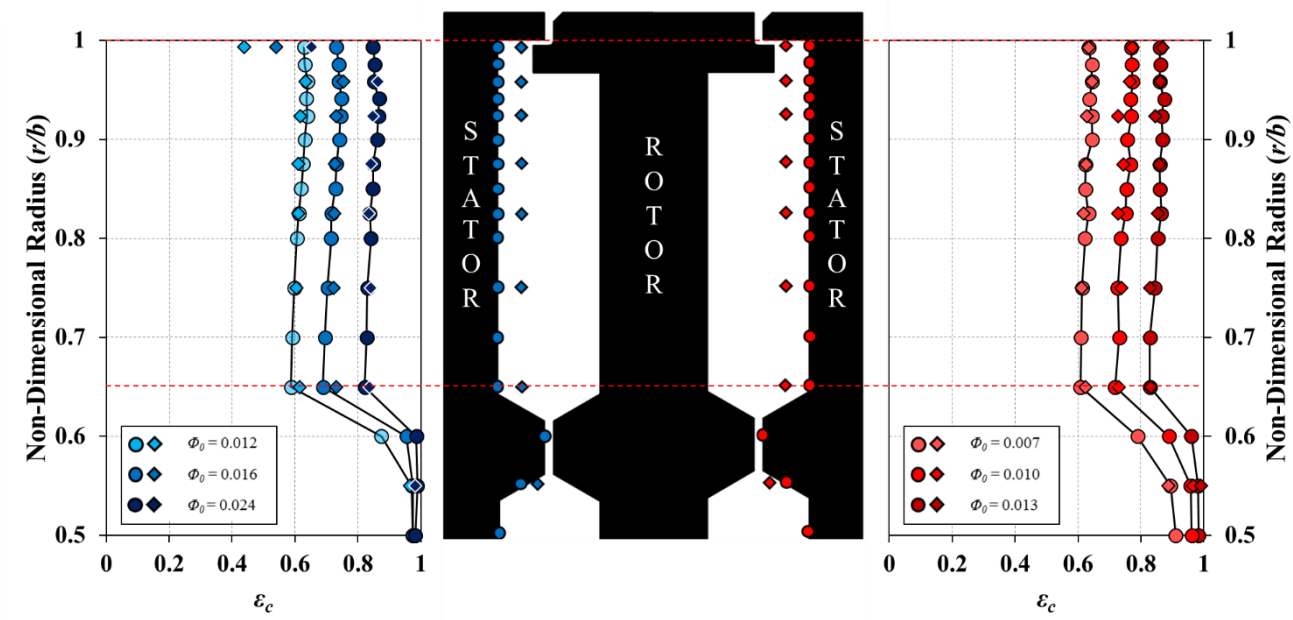

Figure 8: Effect of sealing flow rate on radial distribution of effectiveness for the single radial-clearance seal in the upstream (left) and downstream (right) wheel-space - circles: stator-wall measurements; diamonds: rotating-core measurements) ($Re_\phi = 7.2 \times 10^5$, $C_F = 0.34$)

Comparing the radial distributions obtained in the upstream and downstream wheel-spaces it can be seen that despite the conditions chosen for the experiments resulting in virtually the same ε_c, the values of Φ_0 are very different. For example, for a value of $\varepsilon_c \approx 0.6$ (light colour symbols) the non-dimensional sealing flow rate supplied to the downstream wheel-space is significantly less than that required for the same effectiveness value upstream. In other words the performance of the same seal geometry in the downstream wheel-space is more effective than in the upstream side; this suggests that a weaker driver for ingress exists downstream.

Variation of Concentration Effectiveness with Sealing Flow

The variation of effectiveness, ε_c with Φ_0 for the single radial-clearance seal in both the upstream and downstream wheel-spaces is shown in Figure 9. The concentration measurements were made on the stator surfaces at r/b = 0.958 and 0.85. In both wheel-spaces, ε_c increases with increasing Φ_0, as the sealing flow pressurises the wheel-space and reduces ingestion through the rim-seal. The data collapse onto single curves, which are independent of rotational Reynolds number, Re_ϕ. As shown in Figure 8, the effectiveness at r/b = 0.958 (dark symbols) and 0.85 (light symbols) are virtually identical. For any value of Φ_0 the effectiveness in the downstream wheel-space is higher than that upstream; this indicates a weaker driver for ingress downstream.

The experimental data are fitted with the theoretical effectiveness equations from Sangan *et al.* (2013) using the maximum likelihood method described by Zhou *et al.* (2012). All sets of experimental measurements demonstrate good agreement with the theoretical values. This is a significant as it shows that the simple orifice model from Owen (2011b) can qualitatively predict ingress not only to an upstream wheel-space where the externally-induced ingress is dominated by the steady-state pressure asymmetry from the vanes, but also downstream where ingress is the results of a less powerful driving mechanism.

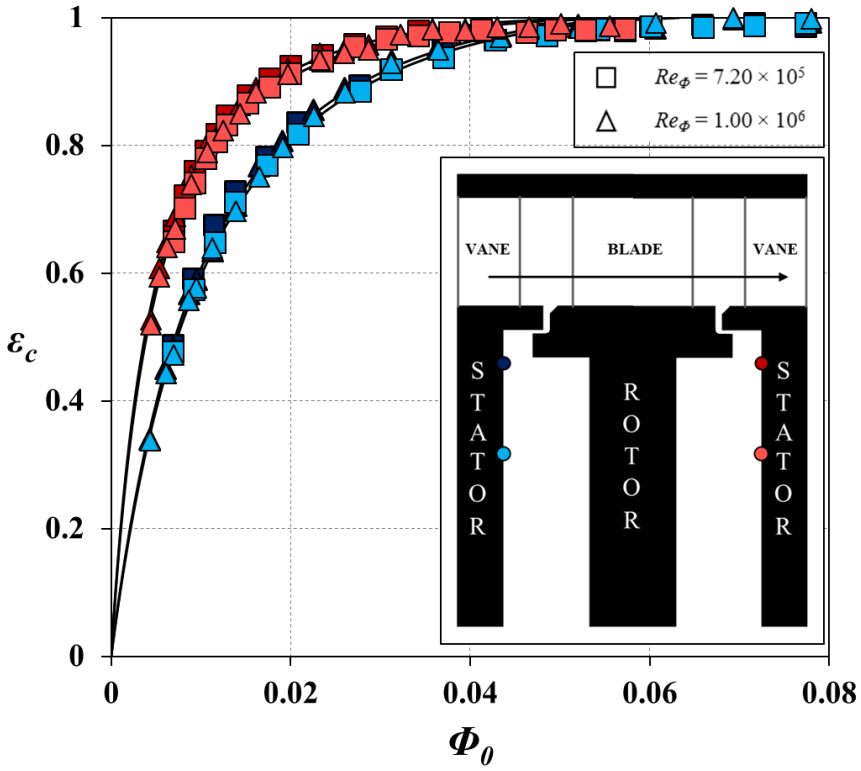

Figure 9: Variation of ε_c with Φ_0 for single radial-clearance seal in the upstream (blue symbols) and downstream wheel-space (red symbols) at r/b = 0.958 (dark symbols) and 0.85 (light symbols) (C_F = 0.34) (symbols denote data; lines are theoretical curves)

CONCLUSIONS

This paper describes a highly versatile, 1.5-stage axial-turbine research facility used to experimentally model ingress into both upstream and downstream wheel-spaces. The rig was specifically designed for detailed instrumentation access in a fluid-dynamically-scaled environment offering an efficient, flexible and relatively inexpensive means of assessing new rim-seal design concepts.

Steady static pressure measurements were made in the annulus at various axial positions both upstream and downstream of the rotor blades for a range of C_F conditions. The upstream locations showed that $\Delta C_p^{1/2}$ increases linearly with C_F whereas downstream $\Delta C_p^{1/2}$ reached a minimum at a flow coefficient close to the operating point.

Measurements of CO_2 tracer gas concentration in both wheel-spaces showed that the effectiveness in the core was equal to that on the stator wall and all distributions were virtually invariant with radius. The sealing flow rate required to seal the downstream wheel-space was found to be significantly lower than that required upstream; this indicates a weaker driver for ingress exists downstream of the rotor blades.

REFERENCES

Childs, P. R. N., 2011, Rotating flow, Oxford: Butterworth-Heinemann.

Daily, J.W. and Nece, R.E., 1960, "Chamber Dimension Effects on Induced Flow and Frictional Resistance of Enclosed Rotating Discs," *Journal of Basic Engineering,* 82(1), 217-232.

Owen, J.M. and Rogers, R.H., 1989. *Flow and Heat Transfer in Rotating-Disc Systems.* Taunton, Somerset, England: Research Studies Press Ltd.

Owen, J. M., 2011a, "Prediction of Ingestion through Turbine Rim Seals. Part I: Rotationally Induced Ingress," ASME J. Turbomach., 133(3), 031005.

Owen, J. M., 2011b, "Prediction of Ingestion through Turbine Rim Seals. Part II: Externally Induced and Combined Ingress," ASME J. Turbomach., 133(3), 031006.

Patinios, M., Scobie, J.A., Sangan, C.M., Michael Owen, J. and Lock, G.D., 2016, "Measurements and Modeling of Ingress in a New 1.5-Stage Turbine Research Facility," *Journal of Engineering for Gas Turbines and Power,* 139(1), 012603.

Sangan, C. M., Pountney, O. J., Zhou, K., Wilson, M., Owen, J. M. and Lock, G. D., 2013, "Experimental Measurements of Ingestion through Turbine Rim Seals. Part 1: Externally-Induced Ingress," ASME J. Turbomach., 135(2), 021012.

Scobie, J. A., 2014, "An Experimental Study of Gas Turbine Rim Seals," PhD thesis, University of Bath.

Scobie, J.A., Sangan, C.M., Michael Owen, J. and Lock, G.D., 2016, "Review of Ingress in Gas Turbines," *Journal of Engineering for Gas Turbines and Power,* 138(12), 120801.

Zhou, K., Wood, S.N. and Owen, J.M., 2012, "Statistical and Theoretical Models of Ingestion Through Turbine Rim Seals," *Journal of Turbomachinery,* 135(2), 021014.